ISIJ International, Vol. 54 (2014), No. 2, pp. 266–274

Simulation of Horizontal Centrifugal Casting: Mold Filling and Solidification

Jan BOHACEK,[1)]* Abdellah KHARICHA,[2)] Andreas LUDWIG[1)] and Menghuai WU[2)]

1) Dept. of Metallurgy, Montanuniversitaet Leoben, Franz-Joseph Strasse 18, Leoben, 8700 Austria.
2) Christian Doppler Lab for Advanced Simulation of Solidification and Melting, Dept. of Metallurgy, Montanuniversitaet Leoben, Franz-Joseph Strasse 18, Leoben, 8700 Austria.

(*Received on July 8, 2013; accepted on November 28, 2013*)

In order to simulate the mold filling and solidification of the outer shell of large work rolls being cast by horizontal centrifugal casting, the shallow water equations were adopted to solve the 2D average flow dynamics of the melt spreading inside the cylindrical mold. The model accounts for centrifugal force, Coriolis force, shear force, gravity and convective and diffusive energy transport. The solidification front was tracked by fulfilling the Stefan condition. Radiative and convective heat losses were included from both, the free surface and the outer wall of the mold. By introducing a stochastic factor to account for the irregular filling jet behavior an uneven spreading of liquid from the center of the mold towards the extremities was predicted. Thus, the formation of the first solid layer also happens unevenly. However, when the mold is covered everywhere with a solid layer, the solidification rate decreases and further filling increases the height of the liquid layer. With increase liquid height the amplitude of the free surface waves also increases.

KEY WORDS: horizontal centrifugal casting; work roll; shallow water equations; Coriolis force; Stefan condition; mold deformation.

1. Introduction

The centrifugal casting process has two distinct branches, the vertical and horizontal centrifugal (or spin) casting, where vertical and horizontal define the placement of the axis of revolution of the mold. The vertical centrifugal casting is commonly used for casting non-cylindrical parts such as valves, propellers, sprockets *etc*. On the other hand, cylindrical parts such as pipes, sleeves, tubes are cast using the second technique provided that the length of the casting is greater than the diameter and that the casting contains a cylindrical bore through. The main difference between the vertical and horizontal centrifugal casting is in the resultant force acting on the melt. With a vertical mold axis the resultant force is constant, whereas with a horizontal mold axis the centrifugal force is periodically disturbed by the gravity and by inherent vibrations. A common advantage of both centrifugal casting processes dwells in obtaining superior mechanical properties of the products compared to the conventional gravity castings.[1)] Now, putting the vertical centrifugal casting[2)] aside, the horizontal centrifugal casting can be discussed in more details. A schematic of the process is shown in **Fig. 1**. The filling starts with the relatively cold mold (~433 K) already rotating at constant rpm (~680 rpm). Solidification occurs immediately, when the melt firstly hits the mold wall. A cloud of fine crystals nucleate close to the mold. Due to the interaction between the forces of inertia and the extreme shear force, nuclei are evenly distributed in the bulk, where they mostly survive and continue growing, which then results in a very fine structure throughout.[3)] Possible columnar crystals solidifying from the mold wall are usually washed out by severe tangential forces and further support the fine structure. Next, the centrifugal force can easily exceed 100 G in magnitude, which helps to suppress the shrinkage and pushes possible inclusions and impurities towards the mold center due to the density difference. The second phenomenon enhancing mechanical properties is the inherent vibration, which promotes the solidification rate and enhances turbulence. The angular frequency Ω has to be carefully chosen. Too low Ω causes the liquid to fail to adhere to the mold wall, which is known as "raining" *i.e.* a curtain of metal droplets falling down from the top of the

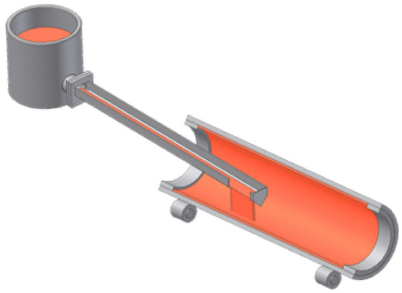

Fig. 1. A schematic of the horizontal centrifugal casting of an outer shell of a large work roll. (Online version in color.)

* Corresponding author: E-mail: jan.bohacek@unileoben.ac.at
DOI: http://dx.doi.org/10.2355/isijinternational.54.266

mold.[4] On the other hand, excessive angular frequencies generally lead to inadmissible strong vibrations, which may result in longitudinal cracks caused by the hoop stress in the initially solidified shell. Besides, even for very little density difference between two alloy elements a too high angular frequency Ω can result in significant segregation.[5] For this reasons, the angular frequency Ω along with many other process parameters such as the pouring temperature, pouring rate, the way how the melt is poured *etc.* require an optimal control.

Some papers written by other researchers on this topic were oriented on the experimental trials, usually some cold experiments; some papers were dealing with mathematical models and numerical simulations. A paper[6] describing various flow regimes during the horizontal centrifuging was done to study the influence of the angular frequency Ω and the liquid height h on waves appearing on the free surface. It was surprisingly found that with increasing the angular frequency the free surface was more disturbed mainly due to inherent mechanical vibrations. For low Ω the free surface formed purely cylindrical pattern. With increasing Ω a free surface pattern was passing through the regime with helical waves, then orthogonal, and eventually "orange skin" waves. Mathematical formulas were stated for vibrations and axial deformation of the mold to analytically investigate free surface patterns. Recently, in-situ experiments were performed,[7] in which the Succinonitrile-1 mass% water alloy was poured in the rotating glass cell and the movement of the equiaxed crystals was observed by means of the high-speed camera. They found that the relative path of the arbitrarily chosen equiaxed crystal associated with a fix point on the mold oscillates and travels in the anti-rotational direction. This phenomenon can be attributed to the interaction between the inertia of the crystal and the 3D flow influenced by effects of the gravity and vibrations. Very interesting experimental work[8] comparing mechanical properties of the Al–Si specimens cast using the centrifugal and gravitational casting technique was done revealing that the tensile and rupture strength was increased for the centrifugal castings. The authors claimed that it is possible to split effects of the centrifugal force into three separate mechanisms: the centrifugal pressure, the inherent vibration, and the fluid dynamics.

In addition to these experimental works, not many numerical studies were devoted to the horizontal centrifugal casting. In,[9] a full 3D simulation of the horizontal centrifugal casting was performed in the commercial software STAR-CD V4 using the VOF method to track the free surface. The whole cylindrical domain was meshed with rather coarse polyhedral elements, which allowed notably large time step (~0.01). Only the flow was solved without taking into account the heat transfer and solidification. Results from simulations showed roughly how the melt is spreading during the filling, but no details are given on how the filling was realized and whether the model could capture some free surface patterns or not. Next, a solidification model[10] was developed for a description of the centrifugal casting process of a metal matrix composite reinforced by dispersed ceramic particles. The numerical model ignored the flow, but forces acting on the particles were taken into account by means of solving ODE for the force balance. A planar solidification front was considered. A study on a similar topic[11] was performed, in which the solidification of the centrifugally cast particle reinforced metal matrix composite was influenced by the particles travelling through the liquid metal matrix. From the force balance on the particle, they found that the Coriolis force can be disregarded when the particle diameter d or the angular frequency Ω is small. In other words, the Coriolis force can be only neglected when the ratio between the coefficient $2\rho_P V\Omega$ (related to the Coriolis force) and the coefficient $6\pi\mu d$ (related to the drag force) is much smaller than unity. In general, the Coriolis force cannot be however neglected. A full 3D numerical model[12] of the horizontal centrifugal casting was recently introduced simulating the interface between the metal and air reconstructed by the VOF method for tracking free surfaces. The main goal was to study the effect of two different filling systems on the temperature distribution on the outer wall of the mold. It was found that with the filling arm moving to and fro more uniform temperature distribution can be achieved compared to the classical static filling. Another numerical study[13] concerning the horizontal centrifugal casting namely casting of pipes was done using the commercial CFD package FLOW3D. In order to avoid extremely low time steps, momentum equations were solved in the rotating frame of reference. However, due to a very small wall-to-length thickness ratio, one simulation still took considerably long time (~20 days).

Nowadays, the commercial CFD packages are along with hyper-threading computing very powerful tools, which can be successfully used to simulate many physical and engineering processes. However, the importance of the proper choice of the equations to be solved and how it should be solved still remains inarguable. In this particular case of the horizontal centrifugal casting of a work roll we believe it is practically impossible to simulate the full casting process (~35 min) by solving the full 3D Navier-Stokes equations for two immiscible phases (the metal and air) in a reasonable time. On the other hand, we are convinced that the main features of the flow and the whole casting can be reliably captured with the help of the 2D shallow water equations (SWE).[14,15] The original 2D SWE were derived from the 3D N-S equations assuming that the pressure is strictly hydrostatic and that the vertical components in the momentum equation for the radial direction can be ignored. For the characteristic length scale much greater than the characteristic height it is a very good approximation. In our system the order of magnitude of the ratio between the characteristic height (liquid metal height) and the characteristic length scale is 0.01 and thus; the simplification by assuming a shallow water flow is reasonable. It is important to note that no assumption is made about the amplitude of waves. The SWE still retains the nonlinear convective terms from the N-S equations. In general, the SWE are used for modeling purposes in oceanography,[16] river management,[17] and meteorology.

In this paper modified SWE are introduced for simulating the average flow dynamics of the melt inside a horizontally rotating mold. The flow is exposed to some sort of vibrations induced by a poor roundness of the mold (or a mass imbalance) and a mold deformation due to thermal effects. The flow equations are coupled with a solidification model

assuming a microscopically planar solid-liquid interface. The diffusive and convective energy transport is solved in the liquid taking into account convective and radiative heat losses from the free surface. A simple heat diffusion model is applied in the solidifying shell and the mold. In **Fig. 2**, a general configuration demonstrates aspects of the SWE model such as a melt flowing over a solidifying shell, heat transfer to the mold, and heat losses from the free surface and the outer wall of the mold.

2. Model Description

The centrifugal force is evidently the most dominant force (~100 G) always pushing the liquid towards the mold wall. From observations during the real casting the liquid perfectly adhered to the rotating mold even during first stages of the filling. This suggests solving the flow in the rotating frame of reference *i.e.* taking into account fictitious forces such as the centrifugal force and Coriolis force. The SWE were derived in the Cartesian coordinate system constructed by unfolding the inner wall of the mold into the *x*-*y* plane, where *x* and *y* denote the axial and the circumferential position. Despite the cylindrical geometry, the Cartesian coordinate system was chosen mainly due to the rather small ratio between the liquid height *h* and the mold radius *R*. The model assumptions are summarized below:

- The momentum equation can be written in the rotating frame of reference due to the high centrifugal force (~100 G).
- The radial momentum is negligible compared to the momentum in the axial and the tangential direction of the cylindrical mold. Higher order terms in the asymptotic series of the static pressure can be neglected and only the hydrostatic pressure is retained.
- A fully developed laminar flow is assumed; therefore, a parabolic velocity profile is forced within the liquid height *h* (Fig. 2) with a no slip boundary condition on the underlying topography and zero stress on the free surface.
- Surface tension effects can be neglected.

The continuity equation remains unchanged for our configuration and takes the form:

$$\frac{\partial(\rho h)}{\partial t}+\frac{\partial(\rho hu)}{\partial x}+\frac{\partial(\rho hv)}{\partial y}=0\ , \quad \text{..... (1)}$$

where *h* is the liquid height, *x* and *y* denote the axial and tangential direction, and *u* and *v* are respective components of mass weighted average of the velocity. In the axial direction, the velocity *u* is defined by:

$$u=\int_{\delta}^{h+\delta}u(z)\,dz\ . \quad \text{..... (2)}$$

The mass weighted average *v* of the velocity in the tangential direction is computed analogically. The momentum equations for both directions *x* and *y* are given by:

$$\frac{\partial(\rho hu)}{\partial t}+u\frac{\partial(\rho hu)}{\partial x}+v\frac{\partial(\rho hu)}{\partial y}+F_{cx}+F_{Cx}=F_{gx}+F_{\tau x} \quad \text{... (3)}$$

and

$$\frac{\partial(\rho hv)}{\partial t}+u\frac{\partial(\rho hv)}{\partial x}+v\frac{\partial(\rho hv)}{\partial y}+F_{cy}+F_{Cy}=F_{gy}+F_{\tau y}, \quad \text{... (4)}$$

where the terms on the left hand side represent the inertia forces including the centrifugal force F_c and Coriolis force F_C. On the right hand side, F_τ denotes the shear force. F_g stands for the gravity force (possibly perturbed by vibrations). Obviously, the centrifugal force acts purely in the radial direction, but its effect emerges in the momentum equations for *x* and *y* direction. Thus, any acceleration acting in the radial direction needs to be firstly expressed as the integral of the equivalent hydrostatic pressure over the liquid height *h*. Then the gradient of such an integral gives the correct *x* and *y* components of the corresponding force. Components of the centrifugal force exerted over the liquid are defined by:[18]

$$F_c=\rho\Omega^2\left(R-h-\delta\right)\nabla\left(h+\delta\right), \quad \text{..... (5)}$$

where *R* is the inner radius of the mold and δ is the height of the solidifying shell. For the derivation of the Coriolis force dependent on the relative velocity we introduce an additional assumption on the velocity profile within the liquid height *h*. We expect the flow to be fully developed laminar. Hence, a parabolic velocity profile was considered with a no slip boundary condition on the wall and zero friction on the free surface. In the case of a perfectly cylindrical mold, the Coriolis force acts only radially and becomes:[18]

$$F_C=\rho\Omega h\left(\frac{5}{2}v\nabla h+2v\nabla\delta+\frac{5}{4}h\nabla v\right) \quad \text{..... (6)}$$

From Eq. (6) it is clear that when the relative motion of the liquid is in the rotational direction, the Coriolis force pushes the liquid towards the mold wall and vice versa. Next, since the relative velocity is maximal on the free surface and zero on the underlying topography, the Coriolis force should be more important at the free surface than on the solid relief. This is indicated by the analytical constants 5/2 and 2 by the terms with the gradient of the liquid height *h* and the solid height δ, respectively. The assumption of a parabolic velocity profile is also used in derivation of the bed shear stress[19] for the Newtonian fluid. The shear force invoked by the bed shear stress acting in the axial direction can be written as:

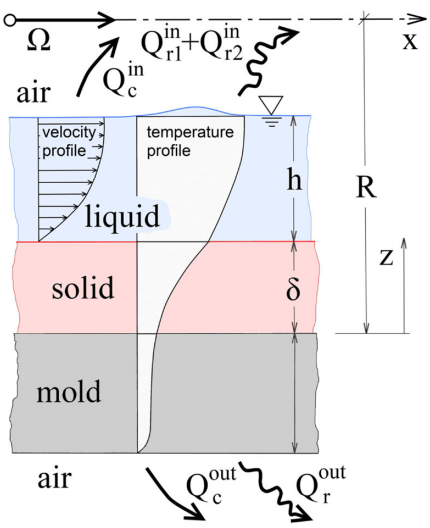

Fig. 2. A schematic of the SWE model. (Online version in color.)

$$F_\tau = -3\mu\frac{u}{h}, \quad \text{..... (7)}$$

where μ is the dynamic viscosity (~0.006 Pa s) and ρ is the density (~6 800 kg/m^3). The shear force in the tangential direction is defined using the same formula (Eq. (7)) except that the velocity component u is replaced by the velocity component v. The shear force F_τ plays an important role and balances the centrifugal force, when the liquid height h diminishes. Finally, the gravity force F_g has components in both x and y directions; however, it is prevailing in the y (tangential direction). In the axial direction the gravity force F_{gx} becomes:

$$F_{gx} = -\rho g h \cos(\Omega t)\frac{\partial(h+\delta)}{\partial x}. \quad \text{..... (8)}$$

In the tangential direction, the component F_{gy} of the gravity force becomes:

$$F_{gy} = -\rho g h\left(\cos(\Omega t)\frac{\partial(h+\delta)}{\partial y} + \left(1-\frac{h}{2R}\right)\sin(\Omega t)\right), \quad \text{... (9)}$$

where g is the gravitational acceleration (~9.81 m/s^2) and t is the current time. In Eqs. (8) and (9), the terms with the slope of the free surface represent the gradient components of the hydrostatic pressure integrated over the liquid height h. In other words, in the SWE these terms correctly reflect the effect of the radial component of the gravitational acceleration g, which has an impact on the flow in both, the axial and the tangential, directions. As already discussed, the real casting is accompanied by inherent vibrations, which are induced by a poor circularity of the carrying rollers or the tracks, and also by deformation of the mold axis due to pouring the hot metal inside the mold. In the numerical model, the vibrations are simply applied by perturbing the gravity force, whereas the mold deformation modifies all other forces except of the shear force F_τ. The mold deformation was realized by assuming the axis following a sine function with the nodes in the position of carrying rollers and the antinode in the center of the mold representing the lowest axial mode shape of a vibrating cylindrical shell.[20] Higher axial mode shapes were not considered in this study. The exaggerated picture of such an imperfect mold is shown in **Fig. 3**. Details on the derivation of the SWE including the influence of the vibrations and mold deformation are given in our papers.[21,22] The first paper[21] is focused on the investigation of free surface patterns influenced by vibrations and axial mold deformations. Free surface patterns were studied on the initially uniform distribution of the liquid height h. Neither the solidification nor the mold filling were discussed. The second paper[22] deals with the solidification of the initially uniform thickness of the liquid and analyses the effect of different heat transfer mechanisms on heat losses from the free surface inside the mold. The mold filling was not included in the model.

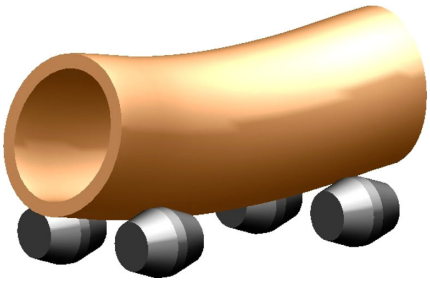

Fig. 3. An exaggerated schematic of the deformed mold for Case B. (Online version in color.)

Concerning the solidification model, we assume that the liquid solidifies exclusively from the mold wall and that there is no slip and also no thermal resistance between the solidifying shell and the mold. Further, it is known that for Prandtl number less than unity, the hydrodynamically fully developed flow is also thermally fully developed. In other words, in our case we believe that the thermal diffusivity is much stronger than the viscous forces; therefore, the thermally fully developed flow is considered. Such a flow is characterized by a parabolic temperature profile (Fig. 1). Further assumptions for the solidification model can be itemized as the following:

- A planar solid/liquid interface is considered between the solid and the liquid (*s/l*). At the current stage of the model, a possible mushy zone is not accounted for.
- The solidifying shell is perfectly attached to the internal mold wall; hence, it rotates with the same angular frequency Ω as the mold. In other words, there is no velocity slip between the mold and the solidifying shell.
- Although a separating refractory material (ZrO_2) is used to separate mold from the casting, a zero thermal resistance is currently considered.
- Heat fluxes are dominant in the radial direction due to the high pouring temperature (~1 755 K) and relatively low initial temperature of the mold (~ 433 K). For this reason, the heat diffusion equation is simplified and solved only in the radial direction. Lateral heat fluxes are neglected.
- Convective and radiative heat losses are modeled inside and outside the mold. During the real casting the mold fronts are insulated by sand cores; therefore, the heat losses from the fronts are neglected.

In the liquid, the heat advection-diffusion equation (Eq. (10)) is solved for the average temperature $\bar{T}$ given by:

$$\bar{T} = \frac{1}{h}\int_\delta^{h+\delta} T(z)\,dz. \quad \text{..... (9)}$$

The heat advection-diffusion equation can be written as:

$$\frac{\partial(h\bar{T})}{\partial t} + \frac{\partial(h\bar{T})}{\partial x}u + \frac{\partial(h\bar{T})}{\partial y}v = \left(\frac{\partial}{\partial x}h\alpha\frac{\partial\bar{T}}{\partial x} + \frac{\partial}{\partial y}h\alpha\frac{\partial\bar{T}}{\partial y}\right) + S_T, \quad \text{..... (10)}$$

where α is the thermal diffusivity and S_T is the source term due to solidification and heat transfer to the mold. In the present study the thermal diffusivity α is kept constant and the same for the liquid, solid, and mold (~5.88e-06 m^2/s). In the future, the effective thermal diffusivity will be implemented in order to account for the variable thermal resistance due to the shell shrinkage[23] and the insulating refractory material (ZrO_2). The *s/l* interface of the solidifying shell is supposed to be planar fulfilling the Stefan condition[24] given by:

$$\rho L_f c = k\frac{\partial T_s}{\partial z} - k\frac{\partial T_l}{\partial z}\ , \quad (11)$$

where L_f is the latent heat (~250 kJ/kg), c is the velocity of the *s/l* interface normal to the interface and the right hand side denotes the net heat flux through the *s/l* interface. The temperature of the *s/l* interface corresponds to the temperature of liquidus T_{LIQ} (~1 586 K).The subscripts s and l denote the solid and the liquid. The thermal conductivity k is constant (~30 W/(m K)) and same for both, the solid and liquid. The same holds for the density. The Stefan condition is coupled with the 1D heat equation, which is solved numerically on each quadrilateral element of the 2D grid and in cylindrical coordinates has the following form:

$$\frac{\partial T}{\partial t} = \alpha\frac{1}{r}\frac{\partial}{\partial r}\left(r\frac{\partial T}{\partial r}\right). \quad (12)$$

Equation (12) describes the heat conduction through the solidifying shell to the mold. Only the 1D heat equation is solved because the lateral heat fluxes are compared to the radial heat fluxes negligible. The Dirichlet boundary condition is applied on the solid/liquid interface (T_l=1 586 K). On the outer wall of the mold the Neumann boundary condition is employed representing convective and radiative heat losses (described below). The convective and radiative heat transfer from the free surface inside the mold was taken into account. The convective losses were simplified by considering a constant heat transfer coefficient HTC_{in} of 100 W/(m^{2}K). Outside of the mold convective heat losses were also accounted for, but due to higher circumferential velocity the heat transfer coefficient HTC_{out} was increased (~150 W/(m^{2}K)). The model of the radiative heat transfer inside the mold is split into two parts. The first part denotes the heat losses via extremities, whereas the second part denotes the heat exchange inside the mold due to the fact that some regions are hotter (or colder) than others. The theory of a black body was applied to simplify the problem.[25] The radiative heat losses via extremities (mold openings) from each surface element were formulated as the following:

$$Q_{r1}^{in} = A\left(1-F_w\right)\sigma\left(T^4 - T_a^4\right), \quad (13)$$

where A is the area of the quadrilateral free surface element, σ is the Stefan-Boltzmann constant (~5.67e-08 W/(m^{2}K^4)), T is the temperature of the free surface and T_a is the temperature of the ambient (~323 K). F_w represents a geometrical resistance or a view factor, which generally depends on the distance between two radiating surfaces and angles between them. Unfortunately, even for this simple case of a cylindrical mold with two openings, the view factor F_w cannot be determined analytically. A numerical approximation of the view factor F_w is however feasible[26] and is given by the polynomial of the fourth order as the following:

$$F_w = ax^4 + bx^3 + cx^2 + dx + e\ , \quad (14)$$

where x is the axial position, which is zero at one extremity. The constants a, b, c, d, and e are –0.1539, 0.7795, –1.502, 1.34, and 0.4981. The constants were determined for the specific case with the mold internal radius R=0.372 m and the mold length L=3.2 m. However, the view factor F_w is related to the actual shape of the free surface inside the mold; therefore, it is time dependent. Qualitatively we can say that as the liquid height h increased during the filling, the radiative heat exchange inside the mold becomes more important, whereas the radiative heat losses via extremities diminish. On the other hand, the percentage rate of change of the view factor F_w is small. Therefore, rather than applying computationally expensive approximation of the constants in Eq. (13) every time step, we accepted a certain error and used the time independent constants a, b, c, d, and e. The summation rule applies for any enclosure; therefore, the view factor F_w can be used to determine the radiative heat exchange inside the mold, which takes the following form:

$$Q_{r2}^{in} = AF_w\sigma\left(T^4 - T_w^4\right), \quad (15)$$

where T_w is the mean surface temperature, which is determined from the energy conservation inside the mold given by:

$$\sum_{i=1} AF_w\sigma\left(T^4 - T_w^4\right) = 0. \quad (16)$$

Using Eq. (15) the mean average temperature T_w becomes:

$$T_w = \sqrt[4]{\frac{\sum F_{iw}T_i}{\sum F_{iw}}}\ , \quad (17)$$

in which we need to evaluate sums of $F_{iw}T_i$ and F_{iw} over all grid elements. The relation for the radiative heat losses from the outer wall of the mold is much simpler, since the view factor from an arbitrary surface element to the ambient is always equal unity. The corresponding formula is given by:

$$Q^{out} = A\sigma\left(T^4 - T_a^4\right). \quad (18)$$

The filling of the mold was realized through a circular mass source in the center of the mold. Since the SWE were solved in the rotating frame of reference, the mass source had to travel in the anti-rotational direction. From the observations during the real casting the momentum of the impinging jet presumably did not have an effect on the initial formation of the liquid ring around the circumference (**Fig. 4**). In addition, the filling jet evidently did not have sufficient momentum to penetrate through the initial liquid ring and come closer to the mold extremities. Therefore, the momentum of the filling jet was ignored in the simulations. The profile of

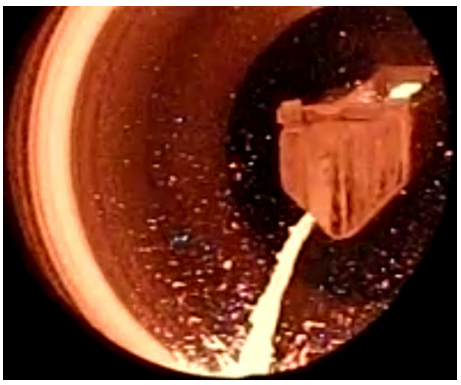

Fig. 4. An early stage of the filling (t<5 s); a filling jet emitting from the filling arm, splashing on the rotating inner wall of the mold (R=0.372 m, Ω=71.2 rad/s), and forming a ring around the mold circumference. (Online version in color.)

the mass source for the filling jet was naturally approximated by a normal distribution with the standard deviation σ estimated from the real casting observations (~90 mm). The real footprint of the filling jet is however far away from a smooth normal distribution. Therefore, the profile of the impingement density was perturbed by means of a Box-Muller transform around the center of the filling jet, which is generally given by:

$$N = \sqrt{-2\ln U_1}\cos\left(2\pi U_2\right), \quad \text{..... (19)}$$

where U_1 and U_2 are randomly sampled numbers from the interval (0, 1]. For a set of U_1, U_2 the resulting N number follows a normal distribution. Using this algorithm the elements in the vicinity of the filling jet center were visited and for each element a number of visits was counted. The ratio between a number of visits and total number of tries gave a strength s of the mass source term S_m, which takes the following form:

$$S_m = 30.2035\left(1-\exp\left(-t\right)\right)\frac{s}{A}, \quad \text{..... (20)}$$

where the time dependent exponential function applies to the variable mass flow rate during the first 5 seconds of the casting, after which the mass flow rate is kept constant of 30 kg/s. Although the end of the filling was not reached in the present simulation results, in the real casting the filling is stopped at t=90 s.

Flow and thermal boundary conditions are summarized in **Table 1**. Second order discretization schemes were used for time and space. The algorithm was stable for the convective condition $CFL \leq 1$. A computational domain for the flow computation consisted of 160×117 (the mold length L × the mold circumference $2\pi R$) orthogonal quadrilateral elements. The heat diffusion in the radial direction was performed on 200 equally spaced grid points. The grid size dependency was tested on a 1D cold flow simulation (without the solidification) of a collapsing liquid column hitting a solid obstacle. The tested number of grid points was 100, 300, and 1 000 s. A wave speed was slightly overestimated for a small number of grid points (100). For a larger number of grid points a wave speed error can be neglected (**Fig. 5**).

3. Results and Discussion

The list of dimensions used in simulations is the following: the length of the mold L of 3.2 m, the internal mold radius R of 0.372 m, and the mold wall thickness of 0.203 m. Material properties and other model settings were mentioned in the previous section. As the initial conditions (t=0 s), we considered an empty mold rotating in the positive direction with the angular frequency Ω of 71.2 rad/s. During the simulation the angular frequency Ω was held constant, although in the real casting especially during the filling a certain drop in Ω is always recorded. At both extremities reflective boundary condition was applied for the flow and zero flux for the enthalpy. Two types of simulations were carried out differing only in the geometrical configuration. The Case A simulation was performed assuming a perfectly cylindrical mold *i.e.* Eqs. (1)–(4) were solved, whereas the Case B simulation was done for a slightly deformed mold with the amplitude of 2 mm at the antinode (Fig. 3). The results are presented on the inner mold wall unfolded in the horizontal plane as depicted in **Fig. 6**.

Table 1. Boundary conditions.

location for BC	flow BC	thermal BC
free surface of the liquid	$\left(\frac{\partial u(z)}{\partial z}, \frac{\partial v(z)}{\partial z}\right) = 0$	Q (convection, radiation)
free surface of the solid	$(u(z), v(z)) = 0$	
dry inner wall of the wall	–	
outer wall of the mold	–	
s/l interface	$(u(z), v(z)) = 0$	$T=T_{LIQ}$
mold extremities	Reflective wall $hu_{GHOST} = -hu$	Q=0 (adiabatic wall)

In the early stage of the filling, when the mass flow rate was still rising according to the exponential function given in Eq. (19) and the cold mold wall was not exposed to the hot liquid yet, the solidification rate is extremely high and newly incoming liquid solidifies almost instantly. In **Fig. 7**, the actual free surface situation is visualized by means of the free surface temperatures at t=0.5 s. The liquid free surface is depicted by the pear-shaped region, from where the position of the jet center is clear (shown as a circle). The filling jet is travelling in the anti-rotational direction. In the neighboring zone the liquid solidified completely; thus, only the solid can be seen. The rest of the surface was not touched by the liquid metal, which is indicated by a significantly lower temperature very close to the initial temperature of the

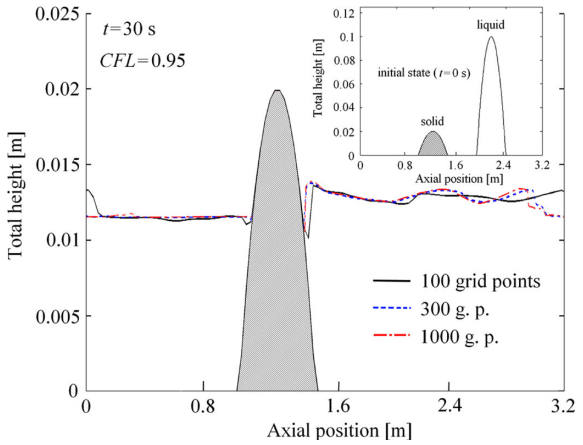

Fig. 5. A free surface of the liquid after a collapse of the liquid column with a wave reflection from the solid obstacle at t=30 s; Initial state (t=0 s) shown in a smaller scale. (Online version in color.)

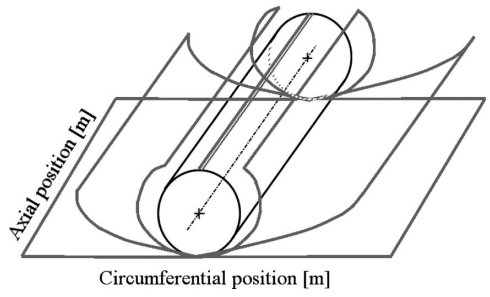

Fig. 6. A cylindrical surface of the inner mold wall unfolded into the horizontal plane.

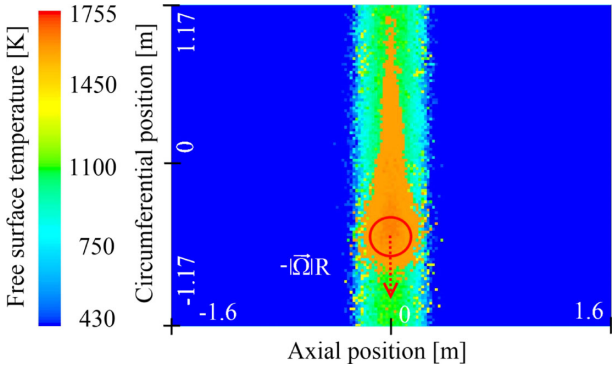

Fig. 7. Contours of the free surface temperature at the early stage of the filling at t=0.5 s with the solid free surface, the liquid free surface, and a dry wall of the mold.; the actual position of the jet is shown as a circle. (Online version in color.)

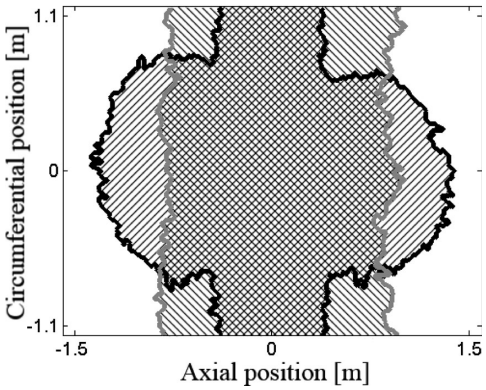

Fig. 8. Position of the moving contact line for results of Case A and Case B at t=6 s shown in grey and black, respectively.

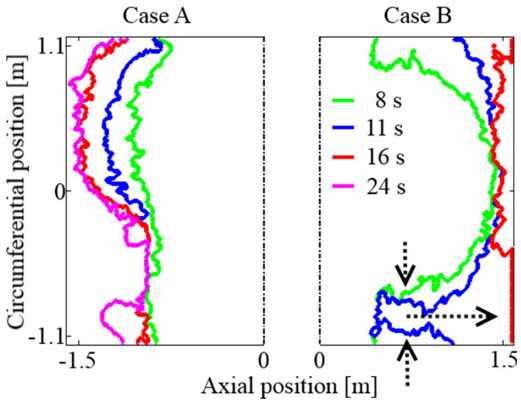

Fig. 9. Actual positions of the contact lines for the Case A and Case B at several time instants. The vertical arrows indicate a tangential spreading of the bulge, whereas the horizontal arrow shows the position and flow orientation of the future dominating filling stream. (Online version in color.)

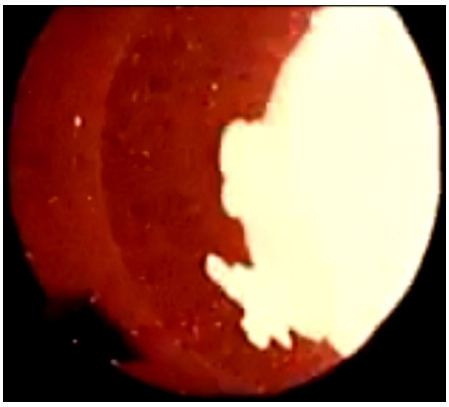

Fig. 10. A snapshot taken during the real casting at approximately t=8 s showing uneven spreading of the melt towards the extremity (a sand core); the filling rate of 30 kg/s, the angular frequency Ω=30 rad/s, the mold radius R=0.372 m, and the mold length L=3.2 m. (Online version in color.)

mold (~433 K). As the solidification and filling proceed, the moving contact lines (where the mold is for the first time being wetted by the metal) are travelling to both extremities with an average speed of around 0.15 m/s. At around 2 seconds the results of Case A deviate from that of Case B. In **Fig. 8**, we compare the actual position of the moving contact line of Case A and B at t=6 s. Obviously, in the case of the perfectly cylindrical mold the moving contact lines remain approximately parallel to the extremities (grey), which does not apply to the case with a deformed mold. Even a very small deformation of the mold (which was considered in Case B), controls the spreading of the melt towards the extremities. Note that we considered only one specific shape of deformed mold. However, this will hold also for many other shapes. The mold extremities are reached at around 10 seconds, however; the way how the extremities are reached is completely different for a deformed mold compared to an ideal non-deformed one. In the Case B nearly symmetric bulges on both sides from the jet continue to grow. Once the bulge touches itself after surrounding the whole circumference, the liquid height increases in that place and high centrifugal force generates a stream that quickly fills up the empty space close to the extremities (see Fig. 8 Case B). Note that the bulge is shifted slightly upwards due to the Coriolis force, which accelerates the liquid relatively moving in the rotating direction and decelerates the liquid moving in the anti-rotational direction. As shown in Fig. 8, in Case A it is small disturbances in the filling jet that are defining the shape of the contact line, and not the deformation of the mold. In the early stage of the casting (Fig. 7), the contact lines are relatively parallel to the extremities. Later, instabilities occur and form regions with bulges and depressions, which then in a random manner proceed towards the extremities (see **Fig. 10** of the real casting). To confirm this random behavior of the liquid spreading, the Case A simulation was run three times. In **Fig. 9**, the asymmetry of the liquid spreading is much more notable for Case A. This asymmetry also causes that in some regions the liquid solidifies completely. Later, a newly coming liquid inundates the solid again and remelting occurs. Such an occurrence of dry regions is shown in grey in **Fig. 11** at t=30 s. The liquid free surface is shown in white. Black dotted arrows highlight the original filling streams whereby the liquid is mainly transported towards the extremities. In **Fig. 12**, a complex wavy relief of the solid/liquid interface is excavated after removing the liquid layer. The position of the filling streams shown in the previous figure now corresponds to the distinct valleys that are a consequence of a reduced solidification rate due to the fresh hot liquid. The same mechanism was applied along the footprint of the filling jet resulting in the formation a pool. Although the solidification starts firstly in the mold center *i.e.* where the filling jet firstly touches the wall, the shell is after some time

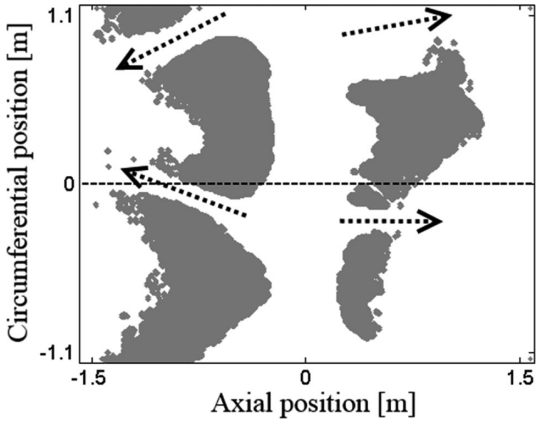

Fig. 11. Dry regions (grey) occurring due to uneven spreading of the liquid towards the left and right extremity for Case A at t=30 s; the liquid free surface shown in white with dashed arrows highlighting the position of the filling streams.

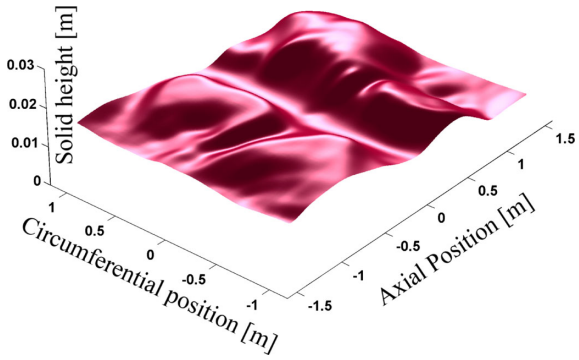

Fig. 12. A 3D relief of the solid/interface for Case A at t=30 s. (Online version in color.)

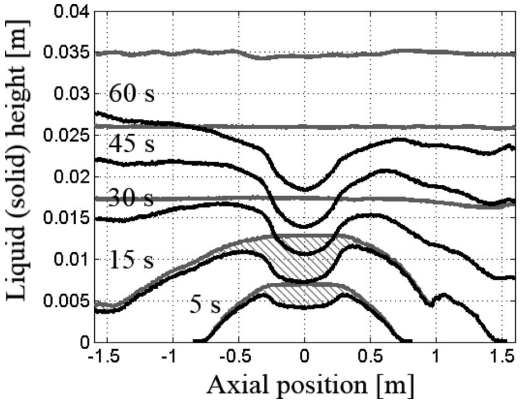

Fig. 13. A time evolution of the solid/liquid interface (black) with the respective liquid free surface (grey) along the axial direction for Case A.

(~30 s) thicker at the extremities. This is mainly caused by the centered position of the filling jet, but also due to increased radiative heat losses at the extremities. A time evolution of the *s/l* interface profile (black) with the respective liquid free surface (grey) is shown along the mold axis (dashed line in Fig. 11) for both Case A and Case B in **Figs. 13** and **14**, respectively. In Case B (Fig. 14), the profile of the *s/l* interface is evidently much more symmetric than in Case A (Fig. 13). Moreover, the pool formed in the center is wider open, which is demonstrated by a two sided arrow in Fig. 14. In addition, on the free liquid surface waves are

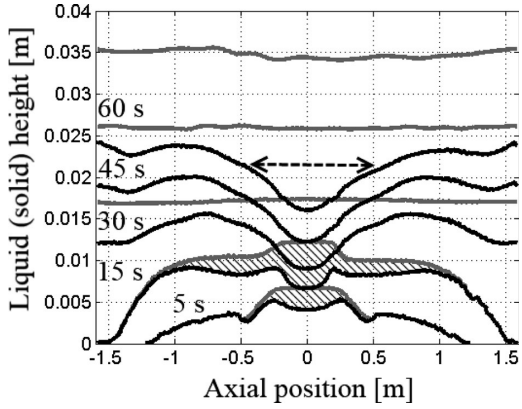

Fig. 14. A time evolution of the solid/liquid interface (black) with the respective liquid free surface (grey) along the axial direction for Case B; The two sided arrow demonstrates a wider pool compared to Case A.

induced by interaction of the forces and the underlying topography, which is more noticeable at later stages of the casting (~60 s) when the liquid height is higher. Various wave patterns appearing on the free surface are beyond the scope of this paper. More details on this topic can be found in our papers.[21,22)]

4. Conclusions

A complexity of a 3D flow during the horizontal centrifugal casting of a large work roll was reduced with the aid of the shallow water equations (SWE) by solving only the axial and tangential velocity components, neglecting momentum in the radial direction, but still resolving the height of the liquid. Using the SWE we save a great amount of the computational power, which consequently allows us to perform parameter studies. The original SWE were modified to account for forces such as the centrifugal force, the Coriolis force, the bed shear stress and the gravity. In addition, a deformation of the mold due to the thermal effects was taken into account assuming a specific shape of the mold (Fig. 3). A simple solidification model was added to the flow equations assuming a dominant heat flow in the radial direction and thus, solving only the 1D heat equation the solid and the mold for each element of the 2D grid. The Stefan condition was applied at the solid/liquid interface to determine its speed. In the paper we focused on the early stage of the casting including the modeling of the filling, which was done by applying a randomly sampled mass source resembling a normal distribution of the impingement density around the jet center. Two different cases were studied, Case A representing a perfectly cylindrical mold and Case B representing a slightly deformed mold. In both cases, the filling jet was responsible for a delayed solidification underneath, which led to the formation of a pool surrounding the circumference. The mold extremities were reached approximately at the same time (~10 s) as during the real casting. However, even in the real casting the liquid does not move towards the extremities uniformly, the contact line forms into finger-like patterns. In Case A, the contact line was more disturbed by the filling jet, whereas in the B) simulation the shape of the contact line was rather controlled by the deformed mold resulting in a more symmetric profile of

the solid/liquid interface along the axial direction. Note that in all simulations a zero thermal resistance was considered in contact between the solidifying shell and the mold. In practice, a refractory material such as ZrO_2 is used to separate the mold from the casting. At the same time, such coating can be used to passively control the heat transfer from the casting by varying the coating thickness along the mold axis. In the present paper only the outer shell (or one layer) was concerned. As a next step we plan to include the second layer (the intermediate layer), which serves as a blending bridge between the outer shell and the gravitationally cast core.

Acknowledgements

Financial support by the Austrian Federal Government (in particular from the Bundesministerium fuer Verkehr, Innovation und Technologie and the Bundesministerium fuer Wirtschaft, Familie und Jugend) and the Styrian Provincial Government, represented by Oesterreichische Forschungsfoerderungsgesellschaft mbH and by Steirische Wirtschaftsfoerderungsgesellschaft mbH, within the research activities of the K2 Competence Centre on "Integrated Research in Materials, Processing and Product Engineering", operated by the Materials Center Leoben Forschung GmbH in the framework of the Austrian COMET Competence Centre Programme, is gratefully acknowledged. This work is also financially supported by the Eisenwerk Sulzau-Werfen R. & E. Weinberger AG.

Nomenclature

A: area of the quadrilateral free surface element (m^2)
c: speed of the solidifying front in radial direction (m/s)
a, c, b, d, e: constant for the analytical expression of the view factor (–)
d: diameter of a particle (m)
F: force (N.m/kg)
F_w: view factor (geometrical resistance)
h: liquid height (m)
HTC: heat transfer coefficient ($W/(m^2K)$)
k: thermal conductivity (W/(m.K))
L: length of the mold (m)
L_f: latent heat of fusion (J/kg)
N: randomly sampled number from a normal distribution (–)
Q: heat flux (W)
r: radial position (m)
R: inner mold radius (m)
s: strength of the mass source (–)
S_m: mass source ($kg/(m^2s)$)
S_T: heat source term (W/m^2)
t: time (s)
T: temperature (K)
T_{LIQ}: temperature of liquidus (K)
u: mass weighted average of velocity in axial direction (m/s)
U_1, U_2: numbers from interval (0, 1] (–)
v: mass weighted average of velocity in tangential direction (m/s)
V: volume of a particle (m^3)
x: axial position (m)
y: tangential position (m)
z: radial position (m)
α: thermal diffusivity (m^2/s)
δ: solid height (m)
μ: dynamic viscosity (Pa.s)
ρ: density (kg/m^3)
σ: Stefan-Boltzmann constant ($W/(m^2K^4)$)
Ω: angular frequency of the mold (rad/s)

Indices:

a: ambient air
c: centrifugal force
C: Coriolis force
g: gravity
$GHOST$: ghost cell
i: cell index
in: inside the mold
l: liquid
out: outside the mold
P: particle
$r1$: radiative losses via extremities
$r2$: radiative heat redistribution inside the mold
s: solid
τ: bed shear stress

REFERENCES

1) G. Chirita, I. Stefanuscu, J. Barbosa, H. Puga, D. Soares and F. S. Silva: *Int. J. Cast Met. Res.*, **22** (2009), 382.
2) R. Zagórski and J. Śleziona: *Arch. Mater. Sci. Eng.*, **28** (2007), 441.
3) S. R. Chang, J. M. Kim and C. P. Hong: *ISIJ Int.*, **41** (2001), 738.
4) K. S. Keerthiprasad, M. S. Murali, P. G. Mukunda and S. Majumdar: *Front. Mater. Sci. China*, **4** (2010), 103.
5) N. Abu-Dheir, M. Khraisheh, K. Saito and A. Male: *Mater. Sci. Eng.*, **A393** (2004), 109.
6) G. Martinez, M. Garnier and F. Durand: *Appl. Sci. Res.*, **44** (1987), 225.
7) H. Esaka, K. Kawai, H. Kaneko and K. Shinozuka: *IOP Conf. Series: Mater. Sci. Eng.*, **33** (2012), 012041.
8) G. Chirita, I. Stefanuscu, D. Soares and F. S. Silva: *Anales de Mecánica de la Fractura*, **1** (2006), 317.
9) K. S. Keerthiprasad, M. S. Murali, P. G. Mukunda and S. Majumdar: *Metall. Mater. Trans. B*, **42** (2010), 144.
10) P. S. S. Raju and S. P. Mehrotra: *Mater. Trans. JIM*, **41** (2000), 1626.
11) L. Drenchev, J. Sobczak, S. Malinoc and W. Sha: *Model. Simul. Mater. Sci. Eng.*, **11** (2003), 635.
12) Z. Xu, N. Song, R. V. Tol, Y. Luan and D. Li: *IOP Conf. Series: Mater. Sci. Eng.*, **33** (2012), 012030.
13) E. Kaschnitz: *IOP Conf. Series: Mater. Sci. Eng.*, **33** (2012), 012031.
14) P. J. Dellar and R. Salmon: *Phys. Fluid.*, **17** (2005), 1.
15) C. W. Hirt and J. E. Richardson: *Flow Sci. Tech. Note.*, **48** (1999), 1.
16) R. J. Leveque: Finite Volume Methods for Hyperbolic Systems, Cambridge University Press, New York, (2002), 429.
17) P. Garcia-Navarro, P. Brufau, J. Burguete and J. Murillo: *Monografias de la Real Academia de Ciencias de Zaragoza*, **31** (2008), 89.
18) A. Kharicha, J. Bohacek, A. Ludwig and M. Wu: to be published.
19) J. Murillo and P. Garcia-Navarro: *J. Comput. Phys.*, **231** (2012), 1963.
20) A. E. H. Love: *Phil. Trans. Roy. Soc. London* (*ser. A*), (1888), 495.
21) J. Bohacek, A. Kharicha, A. Ludwig and M. Wu: Proc. Int. Conf. Experimental Fluid Mechanics, Vol. 2, Technical University of Liberec, Liberec, (2011), 564.
22) J. Bohacek, A. Kharicha, A. Ludwig and M. Wu: *IOP Conf. Series: Mater. Sci. Eng.*, **33** (2012), 012032.
23) E. Panda, D. Mazumdar and S. P. Mehrotra: *Metall. Mater. Trans.*, **37** (2006), 1675.
24) J. A. Dantzig and M. Rappaz: Solidification, EPFL Press, Lausanne, (2009), 134.
25) F. P. Incropera and D. P. DeWitt: Fundamentals of Heat and Mass Transfer, 5th ed., John Wiley & Sons, Hoboken, (2001), 790.
26) J. Bohacek, A. Kharicha, A. Ludwig and M. Wu: to be published.